Juno Waves high frequency antenna properties

Manfred Sampl[1*], Wolfgang Macher[1], Thomas Oswald[1†], Dirk Plettemeier[2], Helmut O. Rucker[1‡], and William S. Kurth[3]

[1]Space Research Institute, Austrian Academy of Sciences, Graz, Austria
[2]Chair in RF and Photonics, Technische Universität Dresden, 01187 Dresden, Germany
[3]Department of Physics and Astronomy, University of Iowa, Iowa City, IA 52242-1479, USA

Key Points:

- High frequency properties of the Waves instrument aboard the Juno spacecraft
- Waves directivity takes arbitrary shapes over receive spectrum
- Waves foot point impedance introduces significant discontinuity loss

*now at: Ericsson EAS, Rosenheim, Germany
†now at: Thomas Oswald Aerospace Software, Weinitzen, Austria
‡now at: Commission for Astronomy, Austrian Academy of Sciences, Graz, Austria

Corresponding author: Manfred Sampl, `manfred.sampl@ieee.org`

Abstract

The Waves instrument aboard Juno is a sophisticated radio astronomy observatory investigating Jupiter's auroral radio emissions and plasma wave interactions. Waves records electrical field properties using two monopole antennas, which are connected to form a dipole. The receiving properties of the Waves dipole changes quite remarkably over the instrument's frequency range from near DC to 40 MHz. In this contribution we outline Waves' electrical sensor properties above the quasi-static frequency range and provide detailed directivity pattern and insertion loss figures of the instrument for science application and data analysis.

1 The Juno mission and the Waves instrument

Juno's overarching science goal is to study Jupiter's origin, internal structure, magnetic and gravity fields, atmospheric composition and explore the polar magnetospheres. The gathered data will improve mankind's understanding of the origin and evolution of our solar system and provide new insights into the Jovian system's planetary formation and evolution. A description of Juno's science goals and objectives can be found on NASA's website, in NASA's Planetary Data System and in Bolton (2018).

The Waves instrument itself is a sophisticated radio astronomy observatory investigating Jupiter's auroral radio and plasma wave emissions. Built as a wave spectrometer, Waves maps Jupiter's electric and magnetic field. Jupiter's polar magnetosphere is charted three-dimensionally by Waves for the first time.

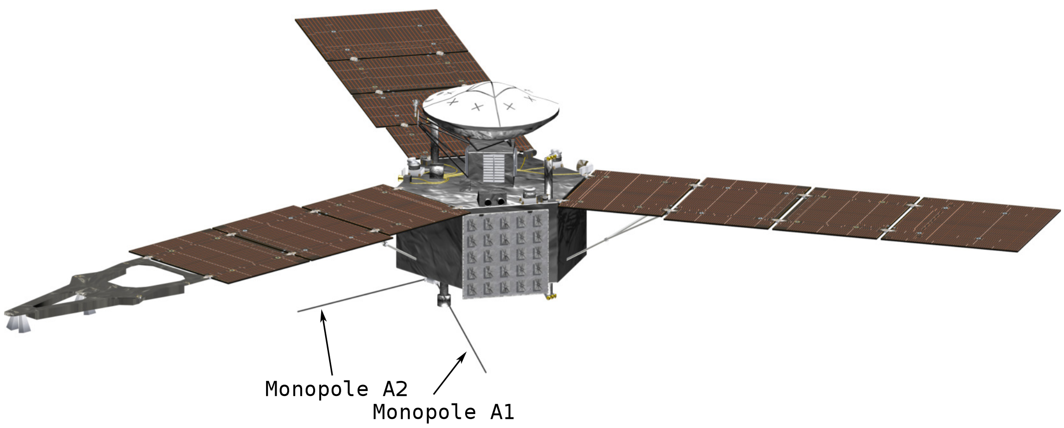

Figure 1. Artist rendering of the Juno spacecraft (©NASA/JPL-Caltech), outlining the Waves monopoles A1 and A2 operating as a dipole.

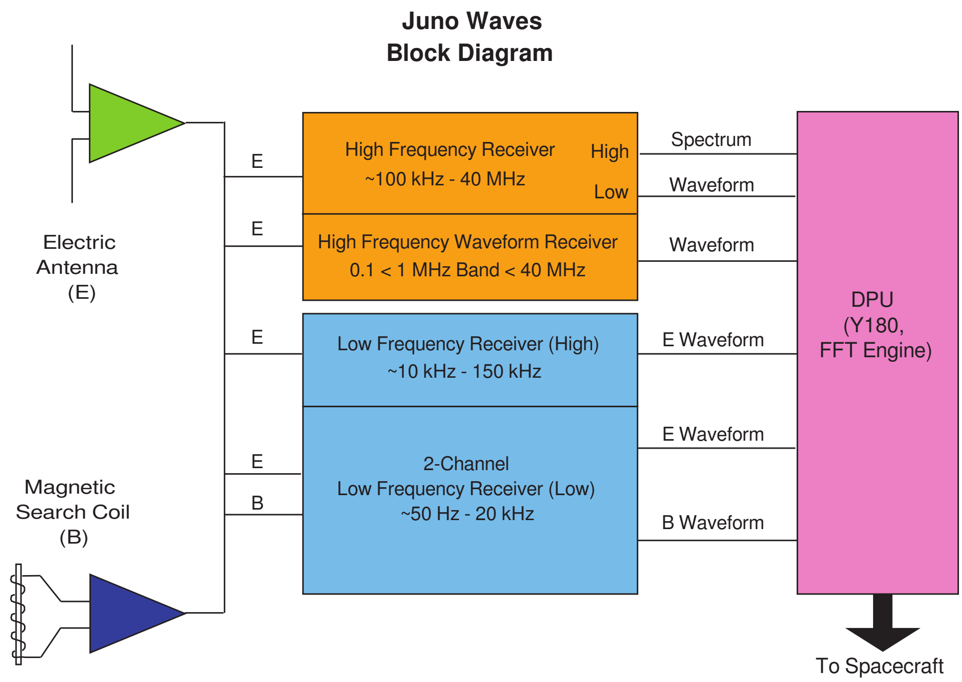

Figure 2. Waves instrument block diagram

Waves records electrical field properties using two monopole antennas (Figure 1), operating as a dipole, and one magnetic search coil, as sensors. The principle of such an instrument has been already explained many times, for example by Gurnett (1998) and in detail for Waves by Kurth et al. (2017). The instrument is in principle a spectrum and waveform receiver as can be seen in block diagram in Figure 2. Basically it consists of pre-amplifiers, filters, receivers for "low" and "high" frequency bands and signal processing units. The instrument is able to record and process electric field strength from 50 Hz up to approximately 40 MHz and magnetic fields from 50 Hz up to 20 kHz. The dynamic range capabilities are especially high due to the challenging demands between low field strength regions in "empty" space and high field strength regions in Jovian source regions, spanning at least 80 dB. A detailed description of the instrument's receiver states and performance can be found in Kurth et al. (2017).

Since the spin stabilized S/C is normally pointing with its high gain antenna to Earth, the Waves dipole is presented to Jupiter and its radio source regions from different angles at any time. Results in section 4 show that for higher frequencies data recorded by Waves is highly dependent on the angular arrival direction of the incident wave. The directivity performance of the Waves dipole changes quite remarkably over the instrument's frequency range from near DC and quasi-static up to 40 MHz. Above the quasi-static range the wavelength of any incident wave has a large impact on the surface current density on the spacecraft leading to individual directivity pattern per frequency. When features on the S/C are in the geometric lengths of e.g. a quarter wave length then the resulting directivity pattern can exhibit pronounced features such as areas of high of "gain".

In the absence of a multi-axial antenna system, source and direction finding investigation have to rely on rotating dipole techniques, which are also directly benefiting from detailed antenna description. To accurately assess a wave phenomena recorded by Waves, it is necessary to acquire Juno's spatial location and orientation for selected points in time, and look-up the dipoles antenna directivity, for the desired direction and frequency, in the provided 3D radiation tables. Additionally it is necessary to look-up Waves' impedance mismatch from the insertion loss table at the desired frequency and factor both into the recorded spectra as archived in the NASA Planetary Data System.

2 Model configuration and numerical computations

The S/C model and computational grid used to calculate the results presented in this contribution have already been described in detail in the companion paper (Sampl et al., 2016) covering the quasi-static part, i.e. the frequency range, where the observed wavelength is larger than the antennas geometrical dimensions. The applied model is directly derived from the S/C manufacturer's CAD and comprises approximately 12,500 triangle mesh elements.

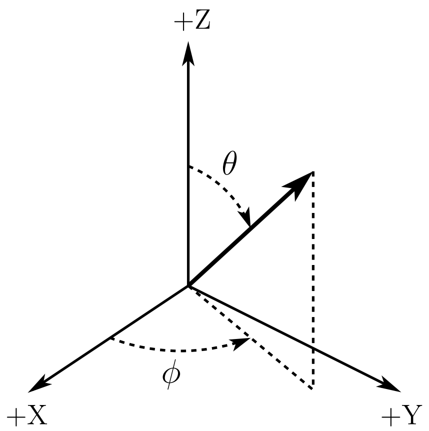

Figure 3. Definition of spherical coordinates θ (co-latitude) and ϕ (azimuth) in the spacecraft-fixed reference frame as used for the representation of antenna axes.

The full-wave solvers FEKO and Concept-II are used to solve the underlying integral equation (c.f. equation (3) in Sampl et al. (2016)) for finding the spacecraft's surface current distribution. From the current distribution the effective length of the dipole can be calculated, as well as other useful parameters such as the antennas radiation pattern and the terminal impedance. Both computational solvers yield identical results within the given digits, leaving any error marginalized. In the following only results from FEKO are presented and used in further post processing.

Figure 3 shows that the z-axis of the spacecraft coordinate system is co-aligned with the high gain antenna axis. The spacecraft x-axis is in the direction of the solar panel which includes the MAG boom at the end. The y-axis completes a right-hand orthogonal system.

3 Waves dipole quasi-static characteristics

Sensor characteristics of electrically short dipole antennas are typically expressed in the present radio astronomy context using the effective length vector and the associated impedance matrix. The description of the antenna properties in this context in explained in detail by Macher et al. (2007); Macher (2014), where the antennas are treated as multi-port scatterer. The Waves' electric sensor results for the quasi-static frequency range, up to 4–5 MHz, are already published in a companion paper (Sampl et al., 2016). The applied spherical spacecraft coordinate system definition is shown in Figure 3, and is identical as in Sampl et al. (2016).

For the sake of completeness we repeat here the results from Sampl et al. (2016) and Kurth et al. (2017), which include the base capacitance of the receiver hardware and stray capacitance from surrounding spacecraft structures.

$$\mathbf{h} = \frac{C_\mathrm{A}}{C_\mathrm{A} + C_\mathrm{b}} \mathbf{h}^\mathrm{o} \tag{1}$$

Kurth et al. (2017) calculates the true length of the effective dipole in (1) resulting in an overall effective length of $\mathbf{h} = 0.46\,\mathrm{m}$ as opposed to the open port effective length of $\mathbf{h}^\mathrm{o} = 1.46\,\mathrm{m}$. In (1) the dipole antenna capacitance of $C_\mathrm{A} = 14.69\,\mathrm{pF}$ is applied together with a rounded base capacitance of $C_\mathrm{b} = 32\,\mathrm{pF}$. The base capacitance is assumed to be the measured per port pre-amplifier input capacitance of $C_\mathrm{b} = 22.15\,\mathrm{pF}$

plus an additional 10 pF for stray capacitances of the antenna foot points' structural assembly and possible cable features.

Due to the findings in this paper, we conclude that the assumptions made for the applied voltage divider in Kurth et al. (2017) are rather pessimistic. In Kurth et al. (2017) the antenna foot points' surrounding structure is added to the base capacitance (additional 10 pF), despite the fact that the surrounding structure is already an integral part of the antenna capacitance, calculated by the applied full-wave solver. Without the additional 10 pF and calculating with the monopole capacitances of 28.50 pF, the total capacitance ratio stays at $C_{\mathrm{A}}/(C_{\mathrm{A}} + C_{\mathrm{b}}) = 28.50/(22.15 + 28.50) = 0.562$ or 4.99 dB. This results in an effective length of about $\mathbf{h} = 0.82\,\mathrm{m}$ when calculating with the open port effective length of $\mathbf{h}^{\mathrm{o}} = 1.46\,\mathrm{m}$. Calculated with the geometric antenna length of 2.41 m, the overall loss is 9.36 dB.

4 Waves directional performance

Previously published results (Sampl et al., 2016) discussed only the lower end of the receivers spectral capabilities. Since the instrument records also observations above some MHz, we now look at the reception properties of the antennas up to their upper end of 40 MHz. The analysis of the frequency range above the quasi-static regime is important, because in-flight calibration which is well applicable for the determination of the quasi-static effective length vectors, is practically infeasible (Cecconi & Zarka, 2005; Vogl et al., 2004)) for frequencies above some MHz. The reason is that a large number of unknowns would have to be determined, since the effective length vector is a complex-valued direction-dependent quantity above the quasi-static frequency range and can not be simplified anymore as defined by Macher et al. (2007); Macher (2014) and applied for Waves as in Sampl et al. (2016).

In the following the choice for characterizing the Waves dipole is shifted from the effective length vector, where the angle of arrival was disregarded in the quasi-static regime, to color coded 3D radiation pattern representing antenna directivity D, which is proportional to the antenna gain G. Such a representation requires the calculation of individual factors of gain or attenuation for discrete angles of wave incidence in the whole spatial domain.

Nevertheless, even above the quasi-static regime it is possible to characterize the antenna properties (in particular for the study of wave polarization) by effective length vectors. For non-quasi-static applications the representation by Sinclair (1950) is usually preferred which defines the effective length vector $\mathbf{h}^S$ normal to the direction of wave incidence. The relation between $\mathbf{h}^S$ and the effective length vector definition $\mathbf{h}$ which becomes direction-independent in the quasi-static limit (often used in low-frequency radio astronomy) is $\mathbf{h}^S = \mathbf{e}_r \times (\mathbf{h} \times \mathbf{e}_r)$ (Macher et al., 2007; Macher, 2014).

Further, textbooks (Balanis, 2005) and literature (Trainotti & Figueroa, 2010) detail how to transform between antenna directivity D, antenna effective area A (the receiving cross section) and the effective length vector $\mathbf{h}^S$ at a given direction of incidence $\mathbf{e}_r$. Thus, we have the relation

$$D = \frac{G}{\eta} = \frac{\pi\zeta_0}{\eta\lambda^2 R_\mathrm{A}} \left|\mathbf{h}^\mathrm{S}\right|^2 = \frac{\pi\zeta_0}{\eta\lambda^2 R_\mathrm{A}} \left|\mathbf{e}_r \times \mathbf{h}\right|^2 \tag{2}$$

Table 1. The maximum receiving directivity D_{RM} of the dipole is stable over the quasi-static frequency range. Via the radiation resistance R_{A} and the dipole the open port effective length $\mathbf{h}^{\mathrm{o}}$, D_{RM} can be calculated via (2), when no further losses are involved.

	Rheometry	Simulation			
freq (kHz)	$\mathbf{h}^{\mathrm{o}}$ (m)	$\mathbf{h}^{\mathrm{o}}$ (m)	D_{RM}	D_{RM} (dBi)	R_{A} (Ω)
300	1.60	1.450	1.50	1.761	1.662E-03
1000		1.399	1.50	1.762	1.718E-02
2000		1.497	1.49	1.751	7.892E-02

where R_{A} is the antenna radiation resistance, η efficiency and $\zeta_0 = 120\pi\,\Omega$ the free space wave impedance. For the present application we can assume $\eta \approx 1$ ($G \approx D$).

In Table 1 a number of selected frequencies have been calculated using (2) to showcase maximum values in the quasi-static regime and interconnect rheometry results (electrolytic tank measurement using a scale model as receiver) in Sampl et al. (2016) with simulation results in the higher frequencies. The necessary input is available from the corresponding simulation results (Sampl et al., 2016), which provide the required antenna radiation resistance R_{A}. Since modern computational solvers yield the antenna directivity D directly such a transformation is generally not necessary.

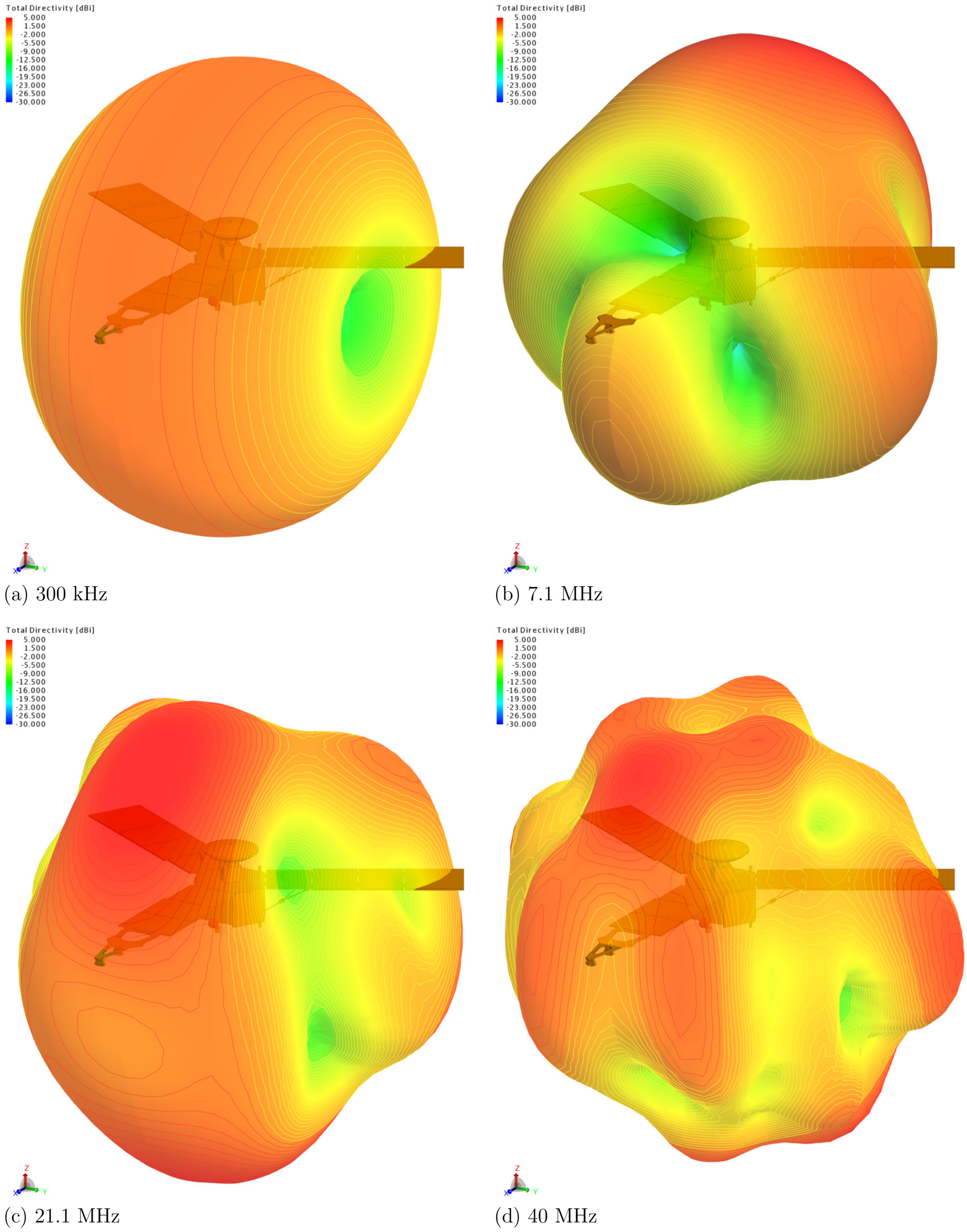

Figure 4. Figures (a)–(b) outline the directional dependence of the Waves dipole radiation characteristic. Below the quasi-static frequency range, in Figure (a), the pattern shows a typical toroidal shape, while above 4–5 MHz the radiation pattern develop multiple elaborate lobes and null directions. For example at 7 MHz a reception maximum in -X direction can be observed, while around 21 MHz the maximum is oriented in the opposite direction +X

The directivity patterns shown in Figure 4 provide a first insight into the complex shapes the directivity of the sensor-dipole assumes at higher frequencies over the spatial domain. All patterns presented are calculated by FEKO with a realistic dipole and S/C layout (CAD configuration 2, section 6 in Sampl et al. (2016)). The reception properties of the dipole, while rather stable at frequencies below some 4–5 MHz, are extremely dependent on the wave incident direction. For frequencies below the quasi-static border, the angular dependence is typically toroidal shaped, but for frequencies above said border the directivity pattern takes arbitrary shapes. Obviously this has a significant impact on the instrument's recorded data. While there are multiple null directions, there are also unexpectedly high directivity values, for a dipole, to be found.

A complete picture of the dipole's reception pattern is provided in the accompanying data package (Sampl & Macher, 2021), as 2D color coded images (co-latitude over azimuth in the S/C reference spherical coordinate system), as well as simple to process raw data tables.

5 Waves antenna input impedance

For further understanding of Waves' reception properties it is necessary to understand the antenna systems impedance performance. The antennas foot point impedance allows together with the pre-amplifiers terminal impedance the calculation of the overall mismatch loss of the antenna–pre-amplifier interface. Besides the antennas effective length and directivity, the impedance mismatch at the dipoles foot point has a significant impact on the recorded power flux.

The antenna systems impedance matrices are readily available from the 3D full wave solver runs as already mentioned in the previous section. The solvers voltage excitation together with the antennas terminal current conveniently yields the complex antenna foot point impedance. These results are usable directly as input for further calculations in section 6.

These results also point out a few interesting features of Waves antenna system. It can be observed that several pseudo-resonances are induced by the geometric properties of the spacecraft. It can be clearly seen from Figure 5 that the resonant behavior of certain geometric features of the spacecraft influence the monopoles and to some certain extent the dipole. The solar panels, which are approximately 9 m long are account-able for a barely visible suppression at approximately 7.5 MHz, mimicking a resonant behavior at 6 MHz. This suppression stems from the fact that, in transmission mode, currents on the solar panels are oriented opposite to the currents on the dipole at about 7.5 MHz. In contrast to that, at 21 MHz the induced currents on the solar panels are oriented in the same way as on the dipole, being responsible for a local resonant effect at around 21 MHz. The lowest proper dipole resonance is usually slightly above the frequency where the imaginary part of the impedance crosses zero, which is found at 26 MHz; similarly, the monopoles show their lowest resonance at 28 MHz.

The immediate effects of these resonances can be seen not only in the impedance plots but also in the directivity patterns in Figure 4.

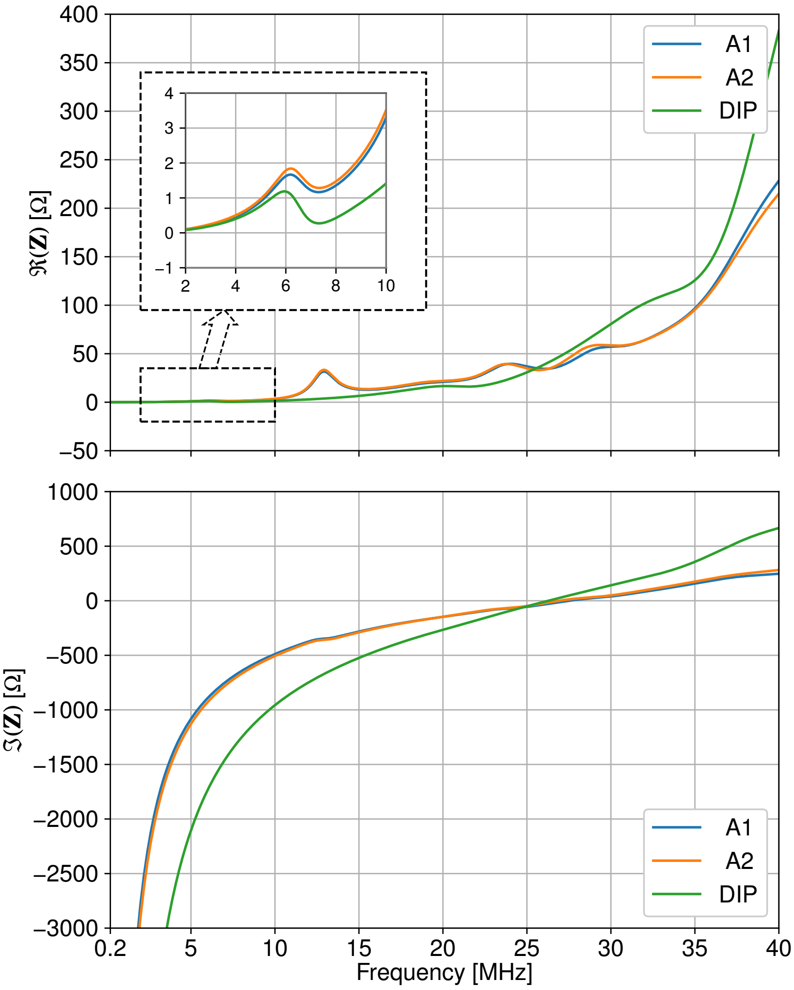

Figure 5. Self impedances of the monopoles A1, A2 and in dipole (DIP) configuration. The shown quantities are the diagonal elements of the impedance matrix as a function of frequency. The upper panel contains the real parts, lower panel the imaginary parts. The curves for the monopoles are nearly identical, which is due to the high symmetry of their deployment on the satellite. The inset in the upper panel outlines pseudo-resonances of the antenna system slightly above the quasi-static area

6 Impedance mismatch loss at the antenna foot point

Since the observation range of Waves extends from near DC to 40 MHz, it is necessary to examine the impedance matching of the antenna and the input amplifier circuit over the sensors frequency range. Such a broadband case poses a substantial challenge for the instrument designers to optimize the antenna–receiver impedance matching and the resulting power or voltage transfer.

In case of the quasi-static range, the discontinuity loss at the antenna foot point is calculated by applying a voltage divider term as in (1). Above the quasi-static border, the dipole foot point impedance is generally not purely capacitive anymore, so it cannot be represented in the form $Y = jwC$ with a real capacitance C.

Therefore we will outline two different approaches to calculate the losses at the antenna foot point. The first approach, derived in section 6.1, is applying a transfer matrix description (Macher, 2014) with the dipole arms treated as individual monopoles A1 and A2, and the measured single-ended input impedances of the pre-amplifier used as load impedances. The second approach, described in section 6.2, is by calculating the differential-mode input impedance of the pre-amplifier from single-ended measurements, as in Carrasco et al. (2012); Bockelman and Eisenstadt (1995) and applying it to the Waves dipole as load impedances.

The input impedance of the Waves instrument pre-amplifier was measured on a flight-like qualification unit using a state of the art network analyzer. Wave's pre-amplifier includes an automatic attenuation capability to increase the dynamic range of the instrument and reduce saturation effects in the receiver. The corresponding data package consists of data sets for each attenuator state "ON" and "OFF". Touchstone format S-parameter files covering the relevant frequency range were provided as input for this investigation.

Both approaches yield similar impedance matching losses, within an acceptable accuracy, taking the applied assumptions and simplifications into account, e.g. disregarding the common mode part in section 6.2. The results, presented in Figure 6 show nicely the frequency dependence of the dipole—pre-amplifier interface. The first observation which can be made is that the lower panel in Figure 6 confirms the calculation as in section 3. The occurring loss is at quasi-static frequencies at 5 dB and then gradually dropping to a zero around 27 MHz. In this area of the spectrum two effect can be observed.

First the real part of the monopole input impedance and the pre-amplifier input impedance is equal at around 50 Ω. Secondly the monopoles resonance frequency is at 27.5 MHz. This circumstances seem to result in a favorable transmission behavior for higher frequencies. Above 27.5 MHz the loss figure turns into negative suggesting a gain situation, with a minimum of -4 dB (or maximum, depending on the perspective) at 35 MHz as per calculation in section 6.1 and -6 dB in section 6.2. This is also the point where the two applied calculation methods show the largest difference of 2 dB. Above 35 MHz the curve swings back to cross zero at 38 MHz ending in 4 dB loss at the upper end of the instruments spectral capabilities. One possible explanation for the occurring negative losses in this configuration is the Ferranti effect. Above the antenna resonance at 27.5 MHz the monopoles impedance turns inductive and together with the capacitive pre-amplifier input, reactive gain could lead to an increased voltage at the receiving pre-amplifier.

The two attenuator states "ON" and "OFF" show the same performance, within the given digits. The results therefore suggest that data post-processing does not need to take the attenuator state into account.

The data package (Sampl & Macher, 2021), which is part of this contribution, contains tables with the insertion loss in 100 kHz steps, from 200 kHz up to 40 MHz, for both cases: attenuator 'ON' and 'OFF'.

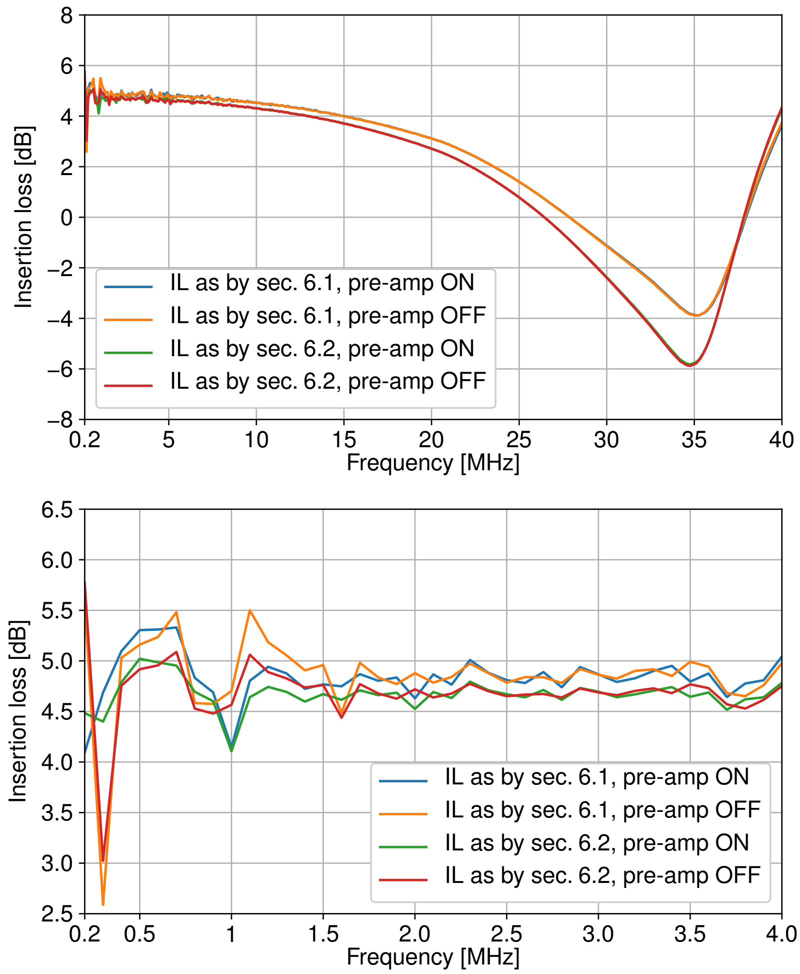

Figure 6. Insertion loss (IL) at the antenna–pre-amplifier interface. The upper panel shows the insertion loss over the full frequency range from near DC to 40 MHz, while the lower panel presents the quasi-static range up to 4 MHz. The lower panel proves that the quasi-static range has a stable performance over frequency; the spikes in the lowest frequency segment can be attributed to the challenging task of performing RF measurements near DC. The upper panel visualizes the frequency dependence of the applicable loss at the investigated interface. For both calculation methods the pre-amplifier state 'ON' and 'OFF' is depicted.

6.1 Insertion loss by impedance and scattering matrix calculation

As we already stated in section 6, for the case of the quasi-static range, the discontinuity loss at the antenna foot point is calculated by applying a voltage divider term as in (1). Above the quasi-static border, the dipole foot point impedance is generally not purely capacitive anymore, so it cannot be represented in the form $Y = jwC$ with a real capacitance C. It is necessary to resort to the general description by means of a complex admittance or impedance matrix which depends on frequency. In this way we take a non-capacitive load as well as possible cross-talk between the ports of the two antenna arms into account. So we describe the load that the antenna system sees when looking from the feed gaps to the receiver (pre-amplifier) by means of a 2×2 load impedance matrix $\mathbf{Z}_\mathrm{L}$. The effective length vectors $\mathbf{h}^{(1)}$ and $\mathbf{h}^{(2)}$ of the dipole arms A1 and A2 , respectively, are subsumed into a transfer matrix $\mathbf{T} = (\mathbf{h}^{(1)}, \mathbf{h}^{(2)})^\mathbf{t}$ (Macher, 2014). Here $(\cdot)^\mathbf{t}$ means the transpose of $(\cdot)$, and the quantities refer to the loaded system (situation in actual deployment, i.e. receiver connected to the antenna arms). Similarly, we define $\mathbf{T}^\mathrm{o} = (\mathbf{h}^{(1)\mathrm{o}}, \mathbf{h}^{(2)\mathrm{o}})^\mathbf{t}$ for the open ports system (receiver disconnected). The relation between $\mathbf{T}$ and $\mathbf{T}^\mathrm{o}$ is given by the matrix equation

$$\mathbf{T} = \mathbf{Q} \cdot \mathbf{T}^\mathrm{o} \tag{3}$$

with the 2×2 matrix

$$\mathbf{Q} = \mathbf{Z}_\mathrm{L} \cdot (\mathbf{Z}_\mathrm{L} + \mathbf{Z}_\mathrm{A})^{-1} \tag{4}$$

Finally, the dipole effective length vector can be determined as the difference between the respective vectors of the monopoles (dipole arms): $\mathbf{h}^\mathrm{d} = \mathbf{h}^{(2)} - \mathbf{h}^{(1)}$ for the loaded ports, and analogously for the open ports, $\mathbf{h}^\mathrm{do} = \mathbf{h}^{(2)\mathrm{o}} - \mathbf{h}^{(1)\mathrm{o}}$. We note that, in general (if $Z_{11} \neq Z_{22}$ and/or $Z_{12} \neq 0$), $\mathbf{h}^\mathrm{d}$ cannot be described as a multiple of $\mathbf{h}^\mathrm{do}$, since the coordinates of the dipole effective length depends on the open port effective lengths of both monopoles:

$$\begin{aligned} h_n^\mathrm{d} &= T_{2n} - T_{1n} \\ &= \sum_{k=1}^{2} (Q_{2k} - Q_{1k})\, T_{kn}^\mathrm{o}, \qquad n = 1 \ldots 3 \end{aligned} \tag{5}$$

However, in the present application we can make the following assumptions: The two monopole terminals are connected to the pre-amplifier in a well balanced way, that is, we can assume $Z_{\mathrm{L}11} \approx Z_{\mathrm{L}22}$, as was confirmed by the results of the network analyzer measurements. Further, there is a mirror symmetry of the spacecraft–antenna system, with the mirror plane running through the middle between the monopole feeds and the plane normal being parallel to the tip-to-tip vector of the dipole, in consequence $Z_{\mathrm{A}11} \approx Z_{\mathrm{A}22}$. This was verified for the quasi-static regime by means of rheometry measurements and simulations (Sampl et al., 2016). Finally, we can apply reciprocity, $Z_{\mathrm{L}12} = Z_{\mathrm{L}21}$ and $Z_{\mathrm{A}12} = Z_{\mathrm{A}21}$. With these simplifications, we find $Q_{21} - Q_{11} = -(Q_{22} - Q_{12})$ and so $\mathbf{h}^{\mathrm{d}}$ becomes, in fact, a multiple of $\mathbf{h}^{\mathrm{do}}$:

$$
\begin{aligned}
\mathbf{h}^{\mathrm{d}} &= \frac{(Z_{\mathrm{L}11} - Z_{\mathrm{L}12})(Z_{\mathrm{L}11} + Z_{\mathrm{L}12} + Z_{\mathrm{A}11} + Z_{\mathrm{A}12})}{Z_{\mathrm{L}11}^2 + 2Z_{\mathrm{L}11}Z_{\mathrm{A}11} - Z_{\mathrm{L}12}^2 - 2Z_{\mathrm{L}12}Z_{\mathrm{A}12} + Z_{\mathrm{A}11}^2 - Z_{\mathrm{A}12}^2}\,\mathbf{h}^{\mathrm{do}} \\
&= \frac{Z_{\mathrm{L}11} - Z_{\mathrm{L}12}}{Z_{\mathrm{L}11} - Z_{\mathrm{L}12} + Z_{\mathrm{A}11} - Z_{\mathrm{A}12}}\,\mathbf{h}^{\mathrm{do}} \qquad (6)
\end{aligned}
$$

where the denominator of the fraction in the first line is the determinant $\det(\mathbf{Z}_{\mathrm{L}}+\mathbf{Z}_{\mathrm{A}})$.

As already stated, the measurements were conducted as simple single-ended two-port measurements, S_{11} giving the reflection coefficient of the pre-amplifier input for A1, S_{22} for A2 and $S_{21} = S_{12}$ being the power transfer between the ports. These parameters define the 2×2 scattering matrix $\mathbf{S}$ from which the load impedance matrix can be determined by Medley (1993)

$$
\mathbf{Z}_{\mathrm{L}} = Z_{\mathrm{c}}(\mathbf{1} - \mathbf{S})^{-1} \cdot (\mathbf{1} + \mathbf{S}) \qquad (7)
$$

where Z_{c} is the characteristic impedance of the connected wave guides and $\mathbf{1}$ denotes the 2×2 identity matrix.

The following procedure can be used to determine the gain (2) as function of direction: First, (7) is applied to obtain the load impedance matrix from the measured scattering parameters for each frequency of interest. Next, $\mathbf{T}^{\mathrm{o}}$ and from it $\mathbf{h}^{\mathrm{do}}$ are determined for all directions (and all frequencies) needed to perform the desired $G(\Omega)$ plot. Finally, formulae (3) and (5) are applied to determine $\mathbf{T}$ and $\mathbf{h}^{\mathrm{d}}$. Provided the mentioned symmetry and reciprocity properties apply, we can omit the determination of the monopole properties (whole transfer matrix $\mathbf{T}$) and directly determine $\mathbf{h}^{\mathrm{do}}$, from which $\mathbf{h}^{\mathrm{d}}$ can be determined via (6). Since we measured S-parameters, it is convenient to write (6) in scattering parameter notation. For that purpose we also introduce the scattering matrix $\mathbf{S}_\mathrm{A}$ of the antenna system, regarded as a two-port consisting of the two monopoles and the spacecraft as a parasitic body. Thus, the relation between $\mathbf{Z}_\mathrm{A}$ and $\mathbf{S}_\mathrm{A}$ is totally analogous to (7). Substitution into (6) and a cumbersome rearrangement (for which we applied *Mathematica*) yield

$$\mathbf{h}^\mathrm{d} = \frac{(S_{\mathrm{L}11} - S_{\mathrm{L}12} + 1)(S_{\mathrm{A}11} - S_{\mathrm{A}12} - 1)}{2(S_{\mathrm{L}11} - S_{\mathrm{L}12})(S_{\mathrm{A}11} - S_{\mathrm{A}12}) - 2}\,\mathbf{h}^\mathrm{do} \tag{8}$$

which are used below for the study of the insertion loss.

Figure 6 shows the frequency dependence of the insertion loss, i.e. the loss due to the inclusion of the base impedance (load including pre-amplifier input impedance, cable and stray capacitance at feed gap which is not taken into account in the antenna model), defined by

$$\mathrm{IL} = -20\log_{10}\left(\frac{|\mathbf{h}^\mathrm{d}|}{|\mathbf{h}^\mathrm{do}|}\right) \tag{9}$$

which can be easily calculated from (6) or (8). In the present context, IL represents the loss in dB of the voltage autocorrelation $|V|^2$ due to the presence of the base impedance.

6.2 Insertion loss from mixed-mode S-parameter calculation

Waves' receiver is built to store data in NASA's Planetary Data System from a dipole antenna. Therefore it seems obvious to not only calculate the impedance mismatch losses via the individual monopoles, but also via the dipole. As the pre-amplifier measurements were conducted as simple single-ended two-port measurements, ($S_{\mathrm{L}11}$ giving the reflection coefficient of pre-amplifier input for A1, $S_{\mathrm{L}22}$ for A2 and $S_{\mathrm{L}21}$,$S_{\mathrm{L}12}$ being the power transfer between both ports) it was necessary to calculate the differential-mode input impedance from the given S-parameter file. Normally it is necessary for a full calculation of the differential input impedance from single-ended measurements to know the mixed-mode S-parameter of the device, containing differential- and common-mode parameters. In the case of a balanced and symmetrical device under test, where the common-mode part is small compared to the differential part, the differential-mode parameters calculation (Carrasco et al., 2012; Bockelman & Eisenstadt, 1995) simplifies to

$$\Gamma_{\mathrm{d}} = \frac{S_{\mathrm{L11}} - |S_{\mathrm{L}}|}{1 - S_{\mathrm{L22}}}. \tag{10}$$

With the given measurements, Γ_{d}, is the differential reflection coefficient of the sought input stage. (10) can be accepted as true, with $|S_{\mathrm{L}}| = S_{\mathrm{L11}} S_{\mathrm{L22}}$, under the assumption that the input stage of the circuit is symmetrical and balanced ($S_{\mathrm{L11}} = S_{\mathrm{L22}}$, $S_{\mathrm{L21}} = S_{\mathrm{L12}}$), and the common-mode part is small compared to the differential part. Fortunately the measurements of the Waves pre-amplifier input stage support the above conditions. By keeping in mind that in the present case $\Gamma_{\mathrm{d}} = S_{\mathrm{d}}$ and by applying bilineal transformation we get the differential pre-amplifier input impedance

$$\mathbf{Z}_{\mathrm{d}} = \frac{Z_{\mathrm{c}}}{2} \frac{\mathbf{1} + \mathbf{S}_{\mathrm{d}}}{\mathbf{1} - \mathbf{S}_{\mathrm{d}}}. \tag{11}$$

From here we can use the same transfer matrix description as in (4), with $\mathbf{Z}_{\mathrm{dip}}$ as dipole foot point impedance and $\mathbf{Z}_{\mathrm{d}}$ as load impedance for the dipole

$$\mathbf{Q}_{\mathrm{d}} = \mathbf{Z}_{\mathrm{d}} \cdot (\mathbf{Z}_{\mathrm{d}} + \mathbf{Z}_{\mathrm{dip}})^{-1}. \tag{12}$$

Finally we can calculate the insertion loss with (9) in the same manner as in section 6.1. Due to the absence of multiple monopole arms the transfer matrix $\mathbf{T}$ simplifies accordingly, and we can write:

$$\mathrm{IL} = -20 \log_{10} |\mathbf{Q}_{\mathrm{d}}| \tag{13}$$

In contrast to $\mathbf{Q}$ as applied in section 6.1, the present approach by applying (10), resulting in $\mathbf{Q}_{\mathrm{d}}$ as in (12), assumes that the mutual impedances $Z_{\mathrm{L12}} = Z_{\mathrm{L21}}$ are negligible in comparison to $Z_{\mathrm{L11}} = Z_{\mathrm{L22}}$.

7 Conclusions

In this contribution we present the directivity of Waves' receiving dipole and the impedance mismatch loss at the dipole's foot point. We show that above the quasi-static frequency range, the instrument's recorded data figures are drastically affected by the wave incidence direction and the wave length, as observed when compared to the true properties of an incident wave.

While the directivity patterns show a typical toroidal shape below the quasi-static border, at higher frequency, arbitrary shapes emerge with several areas of null direction and unexpectedly high values for a dipole ($> 5\,\mathrm{dBi}$). For lower frequencies, Waves' dipole impedance mismatch loss calculations' lie at 5 dB, while for higher frequencies losses decrease up to a minimum of approximately -4 dB around 35 MHz.

For scientific data post processing we recommend to apply the results from the calculations in section 6.1, motivated by the instruments architecture. Afterall the antenna monopoles are independently connected to an impedance transformation stage and from there to the differential interface of an op-amp. This differs quite from the common building practice of dipole antennas, often being connected to the receiver stage via a balun or a similar transformation stage. It can also be stated from the results that the instruments built-in attenuator does not have any noticeable impact on the instruments recorded data and any scientific data post-processing does not need to take the attenuator states into account.

Our work provides the necessary correctional data sets for fully calibrated post-processing of both spectral and spatial analysis of Waves' recorded electrical wave data.

Acknowledgments

Most part of this work was financed by the Austrian Research Promotion Agency (FFG) in the framework of the Austrian Space Applications Program 7 (ASAP-7), project 828273. We thank Dr. Kurth (instrument PI) and the team of the Department of Physics and Astronomy at the University of Iowa for their long-time cooperation and support.

The geometrical and computational model used to compute the results of this contribution is available as supporting information in (Sampl et al., 2016).

The results yielded by this investigation are available as a data package in the Zenodo repository (Sampl & Macher, 2021). It contains files of the Waves' calculated foot point impedance mismatch loss (Data Set 1) and directivity (Data Set 2) over the instrument's whole frequency range in 100 kHz steps. The Plots to Data Set 2 provide images showing for every 100 kHz step a visual 2D-surface impression of the 3D directivity pattern.

References

Balanis, C. A. (2005). *Antenna theory: Analysis and design* (3rd ed.). Hoboken, New Jersey, USA: John Wiley & Sons, Inc.

Bockelman, D. E., & Eisenstadt, W. R. (1995, November). Combined differential and common-mode analysis of power splitters and combiners. *IEEE Transactions on Microwave Theory Techniques*, *43*, 2627-2632. doi: 10.1109/22.473188

Bolton, S. (Ed.). (2018). *The juno mission.* Springer.

Carrasco, C. T., Sieiro, C. J., Lopez-Villegas, J. M., Vidal, N., Gonzalez-Echevarría, R., & Roca, M. E. (2012). Mixed-mode impedance and reflection coefficient of two-port devices. *Progress In Electromagnetics Research*, *130*, 411-428. doi: 10.2528/PIER12052906

Cecconi, B., & Zarka, P. (2005). Direction finding and antenna calibration through analytical inversion of radio measurements performed using a system of two or three electric dipole antennas on a three-axis stabilized spacecraft. *Radio Science*, *40, RS3003*(3). Retrieved from `http://dx.doi.org/10.1029/2004RS003070` doi: 10.1029/2004RS003070

Gurnett, D. A. (1998). Principles of Space Plasma Wave Instrument Design. In R. F. Pfaff, J. E. Borovsky, & D. T. Young (Eds.), *Measurement techniques in space plasmas – fields.* American Geophysical Union, Washington, D.C.: Geophysical Monograph.

Kurth, W. S., Hospodarsky, G. B., Kirchner, D. L., Mokrzycki, B. T., Averkamp, T. F., Robison, W. T., ... Zarka, P. (2017, July). The juno waves investigation. *Space Science Reviews*. doi: 10.1007/s11214-017-0396-y

Macher, W. (2014). Transfer operator theory and inter-reciprocity of non-reciprocal multiport antennas. *Progress In Electromagnetics Research B*, *60*, 169-193. doi: 10.2528/PIERB14051401

Macher, W., Oswald, T., Fischer, G., & Rucker, H. O. (2007). Rheometry of multiport spaceborne antennas including mutual antenna capacitances and application to STEREO/WAVES. *Measurement Science and Technology*, *18*(12), 3731-3742.

Medley, M. W. (1993). *Microwave and rf circuits: Analysis, synthesis and design.* Artech House Inc.

Sampl, M., & Macher, W. (2021, apr). *Juno Waves high frequency antenna properties - data set.* Zenodo. Retrieved from `https://doi.org/10.5281/zenodo.4719832` doi: 10.5281/ZENODO.4719832

Sampl, M., Macher, W., Oswald, T., Plettemeier, D., Rucker, H. O., & Kurth, W. S. (2016, October). Juno model rheometry and simulation. *Radio Science*, *51*, 1627-1635. doi: 10.1002/2016RS005954

Sinclair, G. (1950, Feb.). The transmission and reception of elliptically polarized waves. *Proceedings of the IRE*, *38*(2), 148–151.

Trainotti, V., & Figueroa, G. (2010, Sep.). Vertically polarized dipoles and monopoles, directivity, effective height and antenna factor. *IEEE Transactions on Broadcasting*, *56*(3), 379-409. doi: 10.1109/TBC.2010.2050627

Vogl, D. F., Cecconi, B., Macher, W., Zarka, P., Ladreiter, H. P., Fedou, P., ... Hospodarsky, G. B. (2004). In-flight calibration of the cassini-radio and plasma wave science (rpws) antenna system for direction-finding and polarization measurements. *Journal of Geophysical Research: Space Physics*, *109*(A9), n/a–n/a. Retrieved from `http://dx.doi.org/10.1029/2003JA010261` doi: 10.1029/2003JA010261